J|A|C|S ARTICLES

Published on Web 11/09/2009

Oxygen Reduction on Well-Defined Core−Shell Nanocatalysts: Particle Size, Facet, and Pt Shell Thickness Effects

Jia X. Wang,*,† Hiromi Inada,‡ Lijun Wu,† Yimei Zhu,† YongMan Choi,† Ping Liu,† Wei-Ping Zhou,† and Radoslav R. Adzic*,†

Brookhaven National Laboratory, Upton, New York 11973, and Hitachi High Technologies America, Inc., Pleasanton, California 94588

Received August 10, 2009; E-mail: adzic@bnl.gov; jia@bnl.gov

Abstract: We examined the effects of the thickness of the Pt shell, lattice mismatch, and particle size on specific and mass activities from the changes in effective surface area and activity for oxygen reduction induced by stepwise Pt-monolayer depositions on Pd and Pd_3Co nanoparticles. The core−shell structure was characterized at the atomic level using *Z*-contrast scanning transmission electron microscopy coupled with element-sensitive electron energy loss spectroscopy. The enhancements in specific activity are largely attributed to the compressive strain effect based on the density functional theory calculations using a nanoparticle model, revealing the effect of nanosize-induced surface contraction on facet-dependent oxygen binding energy. The results suggest that moderately compressed (111) facets are most conducive to oxygen reduction reaction on small nanoparticles and indicate the importance of concerted structure and component optimization for enhancing core−shell nanocatalysts' activity and durability.

1. Introduction

Hydrogen fuel cells and electrical vehicles are considered as two promising techniques to cut down carbon emissions and petroleum use.[1] One major obstacle for commercializing fuel cell cars is the high cost of precious-metal catalysts used for the oxygen reduction reaction (ORR) in acid fuel cells.[2] Several strategies have been tried to enhance the Pt mass activity of Pt-based catalysts through increasing effective Pt surface area and intrinsic activity per site.[3] In recent years, Pt monolayer electrocatalysts were synthesized using galvanic displacement of an underpotentially deposited (UPD) Cu monolayer on Pd and other metal or alloy cores that exhibited high Pt mass activities.[4−6] Other highly active ORR electrocatalysts were formed by the segregation upon annealing of Pt_3Ni and Pt_3Co alloys,[7−10] or by dealloying the non-noble metals in PtCu and PtCuCo alloys.[11,12]

A compact Pt surface layer with moderate lattice contraction seemingly is a common structural feature that enhances the ORR activity. Density functional theory (DFT) calculations suggest that the binding strength for reaction intermediates decreases when the lattice contracts,[13−15] which can lower or enhance the catalytic activity depending on whether the adsorption or desorption of the intermediates limits the reaction rate. According to kinetic analysis,[16,17] desorption of O and OH are the rate-limiting steps for the ORR at high potentials on Pt(111) and Pt nanoparticles. Thus, moderate compressive strain in the Pt surface layer enhances its activity for the ORR as demonstrated by the volcano plots for a Pt monolayer on different metals.[18] Questions remain on the uniformity of deliberately made core−shell nanoparticles and how particle size/shape and shell thickness affect surface strain and the ORR activity. Surface relaxation on metal nanoparticles is three-dimensional in nature,

† Brookhaven National Laboratory.
‡ Hitachi High Technologies America, Inc.

(1) Service, R. F. *Science* **2009**, *324*, 1257.
(2) Vielstich, W.; Lamm, A.; Gasteiger, H. A. *Handbook of Fuel Cells: Fundamentals, Technology, Applications*; Wiley: New York, 2003; Vol. 3.
(3) Gasteiger, H. A.; Kocha, S. S.; Sompalli, B.; Wagner, F. T. *Appl. Catal., B* **2005**, *56*, 9.
(4) Zhang, J.; Mo, Y.; Vukmirovic, M. B.; Klie, R.; Sasaki, K.; Adzic, R. R. *J. Phys. Chem. B* **2004**, *108*, 10955.
(5) Adzic, R. R.; Zhang, J.; Sasaki, K.; Vukmirovic, M. B.; Shao, M.; Wang, J. X.; Nilekar, A. U.; Mavrikakis, M.; Uribe, F. *Top. Catal.* **2007**, *46*, 249.
(6) Shao, M. H.; Sasaki, K.; Marinkovic, N. S.; Zhang, L.; Adzic, R. R. *Electrochem. Commun.* **2007**, *9*, 2848.
(7) Toda, T.; Igarashi, H.; Watanabe, M. *J. Electroanal. Chem.* **1999**, *460*, 258.
(8) Chen, S.; Ferrira, P. J.; Sheng, W.; Yabuuchi, N.; Allard, L.; Shao-Horn, Y. *J. Am. Chem. Soc.* **2008**, *130*, 13818.
(9) Stamenkovic, V. R.; Fowler, B.; Mun, B. S.; Wang, G. F.; Ross, P. N.; Lucas, C. A.; Markovic, N. M. *Science* **2007**, *315*, 493.
(10) Stamenkovic, V. R.; Mun, B. S.; Arenz, M.; Mayrhofer, K. J. J.; Lucas, C. A.; Wang, G.; Ross, P. N.; Markovic, N. M. *Nat. Mater.* **2007**, *6*, 241.
(11) Srivastava, R.; Mani, P.; Hahn, N.; Strasser, P. *Angew. Chem., Int. Ed.* **2007**, *46*, 8988.
(12) Yu, C.; Koh, S.; Leisch, J. E.; Toney, M. E.; Strasser, P. *Faraday Discuss.* **2009**, *140*, 283.
(13) Grabow, L.; Xu, Y.; Mavrikakis, M. *Phys. Chem. Chem. Phys.* **2006**, *8*, 3369.
(14) Mavrikakis, M.; Hammer, B.; Nørskov, J. K. *Phys. Rev. Lett.* **1998**, *81*, 2819.
(15) Xu, Y.; Ruban, A. V.; Mavrikakis, M. *J. Am. Chem. Soc.* **2004**, *126*, 4717.
(16) Wang, J. X.; Zhang, J.; Adzic, R. R. *J. Phys. Chem. A* **2007**, *111*, 12702.
(17) Wang, J. X.; Uribe, F. A.; Springer, T. E.; Zhang, J.; Adzic, R. R. *Faraday Discuss.* **2009**, *140*, 347.
(18) Zhang, J. L.; Vukmirovic, M. B.; Xu, Y.; Mavrikakis, M.; Adzic, R. R. *Angew. Chem., Int. Ed.* **2005**, *44*, 2132.

10.1021/ja9067645 CCC: $40.75

considerably differing from that on extended surfaces. While coordination-dependent surface contraction has been demonstrated on 3−5 nm Au nanoparticles,[19] its effect on the catalytic properties of nanocatalysts has not been reported to the best of our knowledge. A better understanding of these issues can facilitate atomic designing of more active and stable ORR nanocatalysts.

In this study, we examined the core−shell nanocatalysts made by Pt monolayer depositions on Pd and Pd_3Co cores using a *Z*-contrast scanning transmission electron microscope (STEM) equipped with an element-sensitive electron energy loss spectrometer (EELS). Detailed analyses were carried out to ensure unambiguous determination of Pt shell thickness and uniformity at the atomic level. Confirmation of atomically ordered core−shell structure encouraged us to carry out the DFT calculations using a nanoparticle model that allows surface atoms fully relaxed in all directions for an in-depth understanding of how the particle's size, lattice mismatch, and Pt shell thickness jointly affect the ORR activity. The new insights gained from this study may have broad implications for better understanding and designing nanocatalysts.

2. Methods

The carbon-supported Pd (10 wt %, ETEK) and Pd_3Co (14% Pd wt, synthesized using colloidal approach[20]) catalysts were used after annealing at 350 °C for 30 min. Their average diameters were 4.0 and 4.6 nm, respectively, determined by X-ray powder diffraction with about 80% particles within ±2 nm size range (Figure S1). These catalysts were dispersed in ultrapure water by sonication and loaded on a polished glassy carbon-disk electrode without Nafion. About 10−40 potential cycles between 0.05 and 1.15 V were carried out in Ar-saturated 0.1 M $HClO_4$ solution until stable voltammetry curves were obtained.

For the atomically resolved STEM and EELS measurements, we used the first Hitachi aberration-corrected STEM (HD-2700C). It is equipped with a cold-field-emission source and a high-resolution Gatan Enfina energy-loss spectrometer. Under its normal operating conditions, we routinely achieve a probe size of 0.1 nm with a 0.4 eV energy resolution. Thus, we could image the PdPt nanoparticles while simultaneously acquiring the Pd- and Pt-distribution maps using their M-edge at atomic resolution. To assist our quantitative analysis, we systematically studied the imaging conditions that affect the high-angle annular dark-field (HAADF) intensity, including the probe's convergent angle, the detector's collection angle, sample thickness, and static and dynamic local atomic displacement. The image calculations were based on the multislice method with frozen phonon approximation using our own computer codes. To compare the calculations with experimental data, we measured imaging parameters using CEOS aberration-correction software and employed a Gaussian point-spread-function (fwhm = 0.1 nm) in the calculation.

All DFT calculations were carried out using the Vienna ab initio simulation package (VASP)[21,22] with the projector augmented wave method (PAW).[23] The generalized gradient approximation (GGA) using the revised Perdew−Burke−Ernzerholf (RPBE) functional[24] was utilized to describe the exchange and correlation energies. To reduce computation time, we constructed a semisphere-like core−shell nanoparticle model (see Figure 4a), placing it in a large enough simulation box to ensure no interactions between nanoparticles. Only the Γ point was used for **k** sampling, and the cutoff energy was 400 eV. Experimentally determined relaxation amplitude for Au nanoparticles rapidly decreases from the top to the second layer, and vanishes beyond.[19] We allowed the shell atoms to fully relax with the core atoms fixed to calculated bulk parameters. The binding energy of oxygen (BE-O) is defined as BE-O = E[NP] + E[O] − E[O-NP], where E[O-NP], E[NP], and E[O], respectively, denote the calculated electronic energies of an adsorbed oxygen species on a nanoparticle, a clean nanoparticle, and triplet O.

3. Results and Discussion

3.1. Pt Monolayer Deposition and Electrochemical Measurements. To generate Pt shells with controlled morphology and thickness on a Pd core, Pd_CPt_n nanoparticles (with n being the number of Pt layers in the shell), we utilized a Cu-UPD-mediated electrodeposition method. Figure 1a shows the voltammetry curves for Cu UPD on Pd and Pt nanoparticle catalysts, wherein a full monolayer of Cu is deposited and removed during potential cycles positive of the Cu bulk's deposition potential (0.36 V). Adding K_2PtCl_4 up to 0.1 mM to such a solution allowed us to irreversibly deposit Pt under diffusion control below its bulk deposition potential (0.67 V). With repeated potential cycles between 0.37 and 0.67 V, the Cu UPD current gradually increases (green curves), reflecting the enlargement of the surface area as the size of the core−shell nanoparticles grows by irreversibly deposited Pt. The role of Cu UPD and stripping cycle in this electrodeposition process is to lower the rate of Pt deposition and to enhance surface diffusion of Pt adatoms so that smooth layer forms.[25,26] At the end of Pt deposition, a linear potential sweep, up to 1 V, completely removes Cu. The number of potential cycles required to deposit a full monolayer of Pt was determined by comparing the rate of increase in measured surface area with the expected values based on the core particles' average diameter. Estimates of Pt loading obtained from averaged Cu UPD stripping charges measured before and after depositing a monolayer yielded a Pt:Pd mass ratio within 15% of the values obtained from measurements of inductively coupled plasma atomic emission spectroscopy.

Following a Pt-monolayer deposition, we measured the ORR polarization (Figure 1c) and voltammetry curves (Figure 1d), respectively, in oxygen- and argon-saturated $HClO_4$ solutions. Repeating the procedure on the same electrode yielded data on the ORR activity as a function of Pt shell thickness. Because there are about 8 atomic layers for a 4 nm sphere-like Pd particle, adding 1−3 Pt layers would increase the surface area by about a factor of $(9/8)^2 = 1.3$ to $(11/8)^2 = 1.9$. The significant increases in effective Pt surface area were measured by integrated hydrogen desorption charge, Q_H, assuming 0.21 mC cm^{-2} based on the measurement using a polycrystalline Pt electrode. Such a set of measurements was also carried out using 4.6 nm Pd_3Co as the core (see Figure S2), which has a slightly contracted Pd surface layer.[6,27] Table 1 lists the specific and mass activities obtained from these experiments with those for 3 nm Pt (because 2−3 nm particles yield the highest Pt mass activity on Pt/C) as the reference. The enhancement factors up to 3 in specific activity, 9 in Pt mass activity, and 2 in the mass activity of the platinum group metals (PGM) illustrate the

(19) Huang, W. J.; Sun, R.; Tao, J.; Menard, L. D.; Nuzzo, R. G.; Zuo, J. M. *Nat. Mater.* **2008**, *7*, 308.
(20) Demortiere, A.; Petit, C. *Langmuir* **2007**, *23*, 8575.
(21) Kresse, G.; Hafner, J. *Phys. Rev. B* **1993**, *47*, 558.
(22) Kresse, G.; Furthmüller, J. *Phys. Rev. B* **1996**, *54*, 11169.
(23) Blöchl, P. E. *Phys. Rev. B* **1994**, *50*, 17953.
(24) Hammer, B.; Hansen, L. B.; Nørskov, J. K. *Phys. Rev. B* **1999**, *59*, 7413.
(25) Brankovic, S. R.; Sieradzki, K.; Brankovic, S. R. *Science* **1999**, *284*, 138.
(26) Wang, J. X.; Ocko, B. M.; Adzic, R. R. *Surf. Sci.* **2003**, *540*, 230.
(27) Suo, Y.; Zhuang, L.; Lu, J. *Angew. Chem., Int. Ed.* **2007**, *46*, 2862.

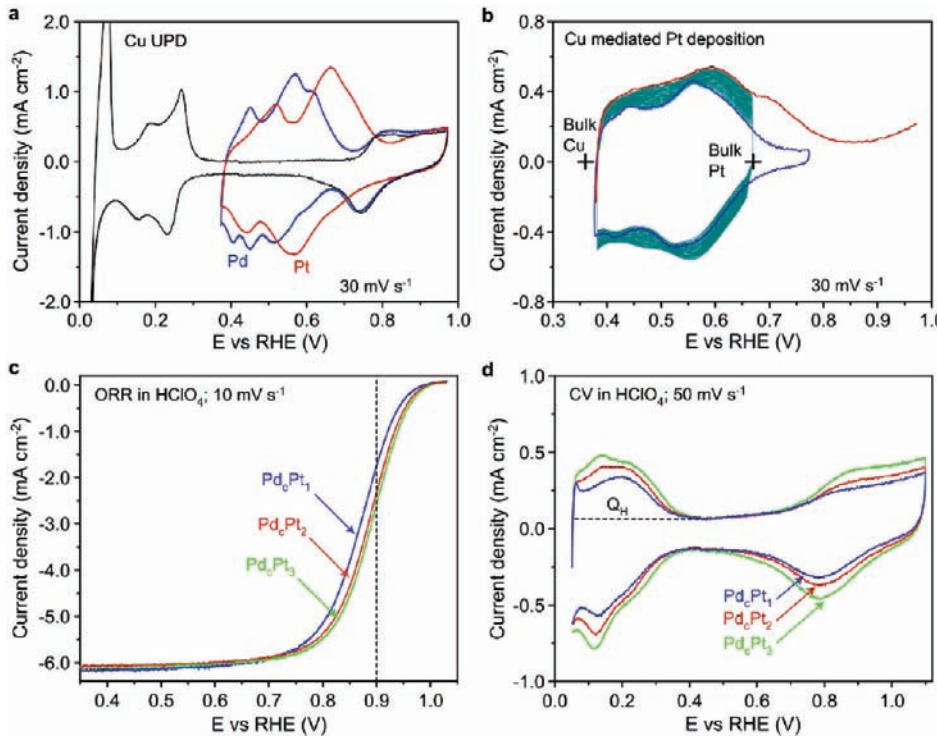

Figure 1. (a) Voltammetry curves for Cu UPD on Pd (blue) and Pt (red) nanoparticles in Ar-saturated solutions containing 50 mM H_2SO_4 and 50 mM $CuSO_4$, together with a baseline voltammetry curve for Pd in a solution without Cu (black). (b) Voltammetry curves before (blue), during (green), and after (red) Pt monolayer deposition on Pd in the above solution with additional 0.1 mM K_2PtCl_4. (c) ORR polarization and (d) voltammetry curves measured for one- to three-monolayer thick Pt shells on carbon-supported Pd nanoparticles (10 wt %, 7 μg cm^{-2} Pd loading) using a rotating disk electrode (1600 rpm) in oxygen- and argon-saturated 0.1 M $HClO_4$ solutions, respectively.

Table 1. ORR Activities at 0.9 V Measured at 10 mV s^{-1} in Oxygen-Saturated $HClO_4$ Solutions as a Function of the Pt Shell's Thickness on Pd and Pd−Alloy Cores (Values for Pt are Included as the reference)

number of Pt layers	specific [mA cm^{-2}]	Pt mass [mA μg^{-1}]	PGM mass [mA μg^{-1}]
	4.0 nm Pd/C (10 wt %)		
1	0.50	0.96	0.25
2	0.52	0.59	0.27
3	0.51	0.43	0.25
	4.6 nm Pd_3Co/C (14 wt %)		
1	0.80	1.56	0.35
2	0.78	0.99	0.42
3	0.79	0.75	0.44
	3 nm Pt/C (20 wt %)		
0	0.25	0.17	0.17

effectiveness of the core−shell approach in enhancing catalytic performance and reducing costs. Similar results were obtained using the galvanic displacement method for Pt deposition.

3.2. Core−Shell Structure Characterization Using STEM-EELS. The atomic structures and component distributions of the Pd_CPt_n nanoparticles were examined using an aberration-corrected STEM equipped with EELS. Figure 2a and b shows atomically resolved HAADF-STEM images for the Pd_CPt_1 and Pd_CPt_4 samples, respectively. The brightness reflects the HAADF intensity that is approximately proportional to the total number of atoms in the column (or the thickness of the particle) and the square of their average atomic number (Z^2). For sphere-like Pd−Pt core−shell particles, a dark center and bright ring may be seen when the shell is more than 3-monolayers thick because Pt has a larger Z than does Pd (78 to 46). However, for a thinner Pt shell, the difference in Z between these two elements is usually not large enough to make the edge brighter because of the lower number of atoms in the column at particle's edge. Furthermore, especially for a monolayer, the static and dynamic displacements (Debye Waller factors) of the Pt atoms on the surface significantly reduce its HAADF intensity. To confirm the Pt shells and determine their thickness, we analyzed the Z-contrast HAADF intensity profiles along the scan lines from the center to the edge, using three-dimensional atomic structural models generated from the observed particles' sizes, shapes, and facets. The black lines in Figure 2c and d fit nearly perfectly to the data. The corresponding structural models indicate that the only surface atoms are Pt for the Pd_CPt_1 sample (Figure 2e) and the Pt shell is 3- or 4-layers thick for the Pd_CPt_4 sample (Figure 2f). For comparison, we show by the green and blue lines in Figure 2c that the intensity calculated using Pd-only models increases monotonously from edge to center. Thus, they could not reproduce the data that exhibit higher intensity at the second peak than that at the third peak from the edge. These analyses confirmed the formation of a well-defined core−shell structure.

Coupling element-sensitive EELS with HAADF images offers another way to determine the thickness and uniformity of the Pt shells. We simultaneously measured the background-subtracted EELS signal for the Pd peak around 420 eV with the HAADF intensity in line scans and two-dimensional mappings, respectively, to determine the sizes and shapes of the Pd core and the entire particle. For a Pd_CPt_2 sample, we show in Figure 3a that the number of Pt layers can be directly counted using the atomic column-resolved line scans. While the HAADF intensity profile exhibits five peaks corresponding to the atomic columns near the particle's edge, the EELS signal decreases sharply around the third one, suggesting a two-layer thick Pt shell. Figure 3b shows a nearly spherical 4.5 nm particle

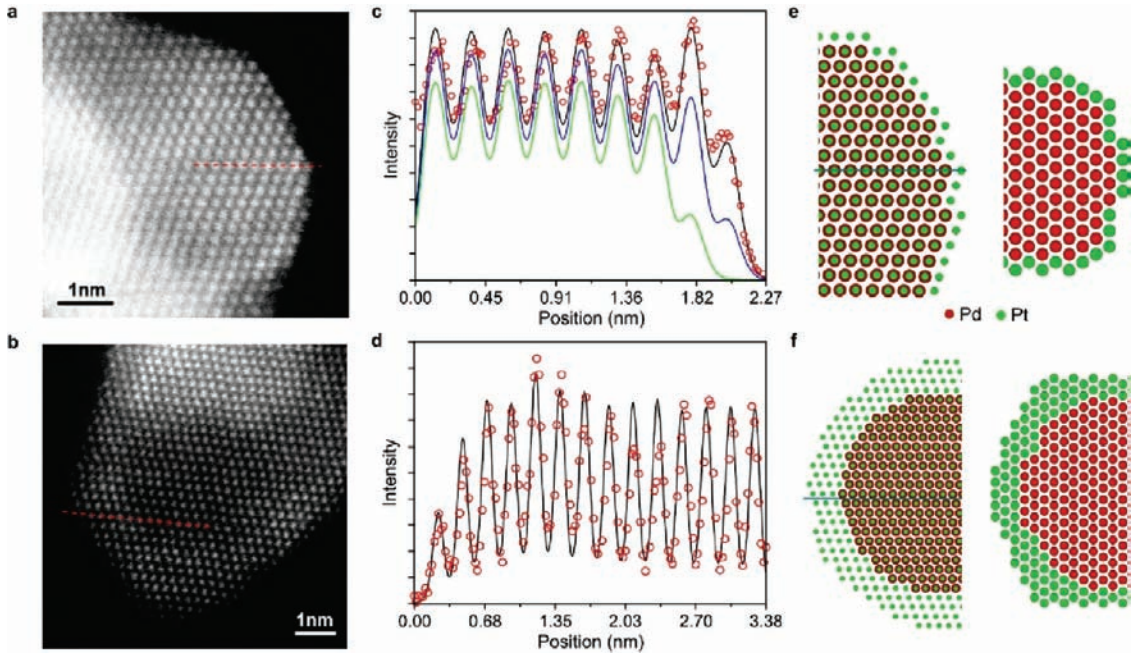

Figure 2. (a,b) HAADF-STEM images of the Pd(core)−Pt(shell) nanoparticles obtained for the Pd_CPt_1 and Pd_CPt_4 samples, respectively. We note that the nanoparticles overlap with the others at the left side in (a), and at the top in (b). (c,d) Intensity profiles (○) from the scan lines (the left ends are defined to be zero on the *x*-axes and the intensity at the nearby vacuum set the zero for *y*-axes) in (a) and (b), and the best fits (black lines), based on the structure models shown in (e) and (f) for Pd particles with 1 and 3−4 Pt surface layers, respectively. The calculations are convoluted with a Gaussian point spread function. Two additional lines in (c) show the calculations made with all of the Pt surface atoms being removed (green line) or replaced by Pd (blue line). (e) Projection of the one-Pt-layer core−shell structure model along the [101] direction (left), and the atomic arrangement (right) of the (1-1-1) plane at the position indicated by the line in the left. (f) Projection of the structure model with 4 Pt layers on the STEM image plane (left) and the arrangements of atoms in the vertical columns along the scan line (right).

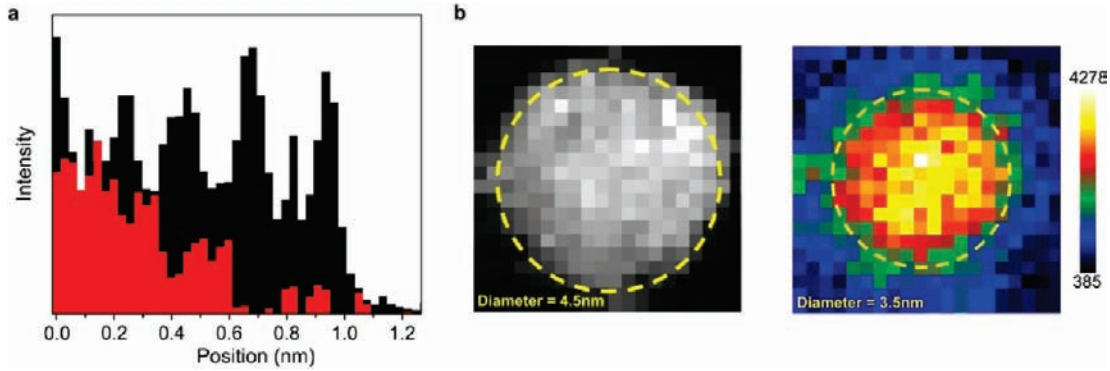

Figure 3. HAADF and Pd EELS intensity profiles for a Pd_CPt_2 sample. (a) Comparison of HAADF (black) and Pd EELS (red) intensity profiles in a line scan. (b) Two-dimensional mapping of HAADF intensity (left) and Pd EELS signal (right) obtained with 0.27 nm/pixel resolution.

with a 3.5 nm Pd core, values obtained, respectively, from the intensity cutoffs in the HAADF and EELS intensities. Because the Pt layer spacing is about 0.24 nm, the 0.5 nm difference in radius confirms the presence of a two-layer thick Pt shell. A quick check using the HAADF-EELS combined line scans for many particles substantiates the overall consistency in thickness of the Pt shell.

3.3. DFT Calculation and ORR Specific Activity on Core−Shell Nanoparticles. To better understand the factors determining the ORR specific activity, we carried out DFT calculations using a semisphere-like core−shell nanoparticle model containing both (111) and (100) facets as shown in Figure 4a. These facets are typical of small fcc metal particles. For example, icosahedrons have only (111) facets, and the cuboctahedrons contain (111) and (100) facets (Figure 4b). Differing from the slab model,[18,28−31] relaxations were allowed in both out-of-plane and in-plane directions for the atoms in the shell. Huang et al. recently reported a coordination-dependent surface atomic contraction on 3−5 nm Au nanoparticles.[19] The out-of-plane contraction was largest for the atoms at the edges, significant at the (100) facets, and smallest in the middle of the (111) terraces, resulting in a significant in-plane contraction at the (111) facets. In agreement with their experimental findings, our DFT calculations for a Pt nanoparticle (using the 1.8 nm Pt_CPt_1 model) demonstrate a considerable decrease in average in-plane spacing on the (111) terraces as compared to that on the extended Pt(111) surface (−4.2%). While this nanosize-induced in-plane contraction decreases with increasing particle size, its effect on the

(28) Ma, Y.; Balbuena, P. B. *J. Phys. Chem. C* **2008**, *112*, 14520.
(29) Nørskov, J. K.; Rossmeisl, J.; Logadottir, A.; Lindqvist, L.; Kitchin, J. R.; Bligaard, T.; Jónsson, H. *J. Phys. Chem. B* **2004**, *108*, 17886.
(30) Nilekar, A. U.; Mavrikakis, M. *Surf. Sci.* **2008**, *602*, L89.
(31) Stamenkovic, V.; Mun, B. S.; Mayrhofer, K. J. J.; Ross, P. N.; Markovic, N. M.; Rossmeisl, J.; Greeley, J.; Nørskov, J. K. *Angew. Chem., Int. Ed.* **2006**, *118*, 2963.

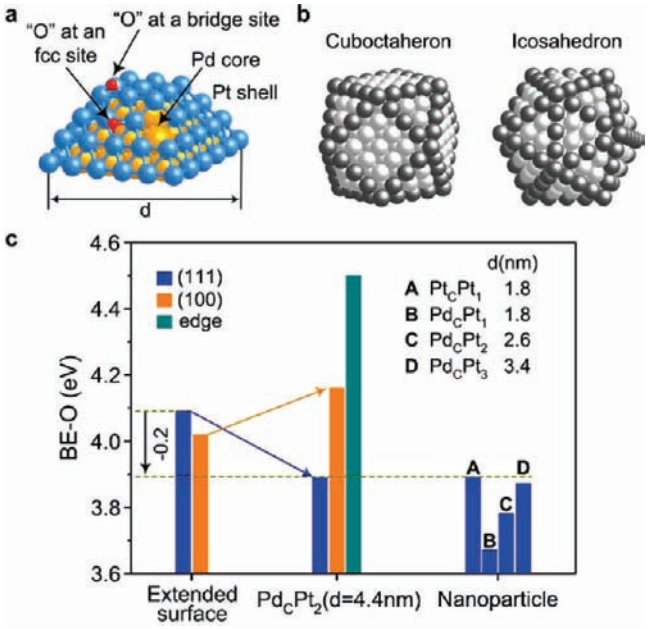

Figure 4. (a) A semisphere-like Pd_CPt_n nanoparticle model used in the DFT calculations with a diameter of *d*. (b) Two sphere-like shapes with different fraction of atoms at facets. (c) Binding energy for oxygen on different sites calculated using the slab model for extended surfaces (as a reference), and the nanoparticle model for various core−shell nanoparticles.

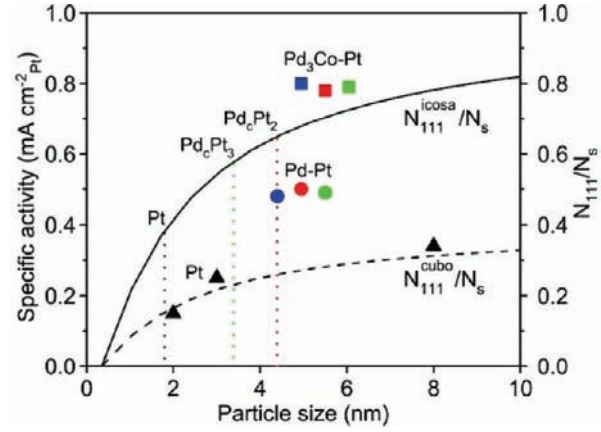

Figure 5. ORR specific activities at 0.9 V measured at 10 mV s^{-1} (symbols, left axis) and surface fraction of atoms on the (111) facets (solid and dashed lines, right axis) as a function of particle size. The vertical dotted lines mark the sizes of three nanoparticle models that have the BE-O close to the optimal value of 3.89 eV. The blue, red, and green colors are used, respectively, for particles with 1-, 2-, and 3-Pt layers.

binding energy for oxygen (BE-O) cannot be ignored for particles up to 5 nm at least.

We further examined the site-dependent BE-O using a 4.4 nm Pd_CPt_2 nanoparticle model. The most stable configuration for O adsorption is bridging adsorption at the edges with a BE-O of 4.50 eV, followed by bridging adsorption at the (100) terraces (4.16 eV), and then fcc adsorption at the (111) terraces (3.89 eV). The −0.27 eV difference in BE-O between the (111) and (100) facets on nanoparticles distinctly differs from that of 0.07 eV on extended surfaces, as indicated by the arrows in Figure 4c. Because slight weakening of the oxygen binding with respect to that on the extended Pt(111) surface enhances the ORR activity,[29−31] the highly coordinated (111) facets are most conducive to the ORR on small nanoparticles.

For the Pd_CPt_n particles, their size and the lattice mismatch (−0.9%) jointly determine the strain that affects the BE-O on the (111) facets. Because the intrinsic ORR activity is largely determined by the BE-O,[29−31] this fact indicates that particle size affects not only the fraction of active sites at surface, but also the turnover frequency (TOF) per active site. The product of the two determines the specific activity. A previous study of the ORR on transition metal alloys suggested that the best ORR electrocatalysts may bind oxygen more weakly, by about 0.2 eV,[31] than does Pt(111), that is, corresponding to 3.89 eV in our calculations (dashed line in Figure 4c). This value is reached on 1.8 nm Pt particles solely by the nanosize-induced surface contraction. Larger particle sizes for optimal BE-O were found using the 3.4 nm Pd_CPt_3 and 4.4 nm Pd_CPt_2 models where reduced nanosize effect is compensated for by increased influence of Pd core. The Pd_3Co alloy has a slightly smaller lattice spacing than does Pd, and thus further shifting to larger size is expected due to the stronger lattice-induced compression.

In light of these findings, we plot in Figure 5 the measured specific activities as a function of particle size, together with the calculated surface fraction of atoms on the (111) facets (N_{111}/N_s) of the icosahedral and cuboctahedral particles. As the dotted vertical lines show, one advantage of the Pd_CPt_n particles is their having the optimal BE-O in the 3−6 nm size range where the N_{111}/N_s is significantly higher than that at 1.8 nm. The large difference in N_{111}/N_s between the two particle shapes suggests the potential of enhancing the ORR activity through shape- and morphology-controlled syntheses. Because low-coordination sites are prone to oxidation and dissolution, ensuring a smooth and (111)-orientation-rich Pt surface bodes well for simultaneously enhancing the ORR catalyst's activity and stability.

4. Conclusions

We demonstrated, using atomic-resolved STEM-EELS images, the synthesis of well-defined core−shell nanocatalysts for oxygen reduction in acid fuel cells. Pt-monolayer catalysts on 4 nm Pd and 4.6 nm Pd_3Co cores exhibited 1.0 and 1.6 mA μg^{-1}_{Pt} mass activities at 0.9 V, respectively, about 5- and 9-fold enhancements over that of 3 nm Pt nanoparticles. The 2- and 3-fold enhancements in specific activity can be mainly attributed to the nanosize- and lattice mismatch-induced contraction in (111) facets based on the DFT calculations using a nanoparticle model. These results point the way to tailoring a Pt shell's structure and properties by controlling core particle's components, size, and shape for further enhancing the activity and durability of the ORR electrocatalysts.

Acknowledgment. This work is supported by the U.S. Department of Energy, Divisions of Chemical and Material Sciences, under Contract No. DE-AC02-98CH10886. We thank the National Energy Research Scientific Computing Center for CPU time, which is supported by the Office of Science of the U.S. Department of Energy under Contract No. DE-AC02-05CH11231.

Supporting Information Available: (1) Particle size determined by X-ray diffraction and STEM for Pd and Pd_3Co nanoparticles on carbon supports; (2) ORR polarization and voltammetry curves measured for one- to three-monolayer thick Pt shells on carbon-supported Pd_3Co nanoparticles. This material is available free of charge via the Internet at http://pubs.acs.org.

JA9067645